Fourier Transform Holographic Associative Processors Based on Bacteriorhodopsin

Article *in* International Journal of Unconventional Computing · October 2012

CITATIONS
3

READS
66

3 authors, including:

Jordan A. Greco
University of Connecticut
23 PUBLICATIONS **114** CITATIONS
SEE PROFILE

Robert R. Birge
University of Connecticut
337 PUBLICATIONS **10,593** CITATIONS
SEE PROFILE

Int. Journ. of Unconventional Computing, Vol. 8, pp. 433–457
Reprints available directly from the publisher
Photocopying permitted by license only

Fourier Transform Holographic Associative Processors Based on Bacteriorhodopsin

JORDAN A. GRECO[1], NICOLE L. WAGNER[2], AND ROBERT R. BIRGE[1,2]*

[1]*Department of Chemistry, University of Connecticut, 55 North Eagleville Road, Storrs, Connecticut 06269-3060, USA; Phone: 860-486-6721; Fax: 860-486-2981*
E-mail: jordan.greco@uconn.edu; rbirge@uconn.edu
[2]*Department of Molecular and Cell Biology, University of Connecticut, 91 North Eagleville Road, Storrs, Connecticut 06269-3125, USA*
E-mail: nicole.wagner@uconn.edu

Received: October 15, 2012. Accepted: October 22, 2012.

We explore the use of the light-transducing protein, bacteriorhodopsin, in optical associative memories and processors. This protein has long been known as an excellent material for photonic applications due to inherent photochemical efficiency and stability. Here, we investigate aspects of complex Fourier association using computer simulations and relate the results to the holographic properties of bacteriorhodopsin-based thin films. For both real-time computing and long-term data storage applications, genetic optimization is necessary to enhance the kinetics and quantum efficiency of the photochemical formation of the blue-shifted intermediates (the **M** and **Q** states) of the bacteriorhodopsin photocycle. Methods in genetic engineering and directed evolution are presented briefly, in addition to a discussion on the design, capabilities, and limitations of protein-based optical associative processors.

Keywords: Bacteriorhodopsin, holography, associative memory, bioelectronics, protein-based processors, biomimetics, complex Fourier association, photochromism, directed evolution

INTRODUCTION

Human creativity and the storage and retrieval of complex information in the brain are based on associative processes. Unlike the serial memories used in silicon computer architectures, humans use associative processing to link and retrieve information. The human brain is capable of matching structured or

unstructured sensory input with memory using a variety of associative processes, many of which remain obscure [1-4]. Accordingly, many computer scientists believe that true artificial intelligence will require the development of large-scale memories that implement associative recall [5].

Associative memories operate very differently than the semiconductor-based memories that dominate current technology. Modern random-access memory (RAM) is address-based, where data are written, read, and erased based on an addressable location. For decades, this architecture has proven to be optimal because it can be implemented using large-scale lithographic technology and is highly reliable. However, such an approach does not lend itself to associative recall. Computer memories that are based on associative recall use a content-addressable memory (CAM) structure, in which the entire memory is searched simultaneously in reference to an input data block. In most implementations, the memory returns the closest match if no perfect match can be found, and will return the data block or data block address necessary to facilitate a more global associative process.

The motivation behind the development of associative memories extends beyond the goal of creating artificial intelligence. Consumer demand for more powerful computing systems has driven the dramatic decrease of the feature size of integrated circuits. Consequently, these devices have already begun to approach the molecular scale and will soon reach the scalable limits of lithographic bulk materials, as predicted by Moore's law [6]. Moreover, packing smaller transistors onto silicon chips in RAM structures has lead to power and heating issues while under operation [7, 8]. To circumvent these problems, new approaches should be explored that provide alternative architectures. There have been many recent advancements in the encoding and manipulation of information at the molecular level, and bioelectronics has shown promise due to the sophisticated control obtained through self-assembly and genetic engineering [9]. Here, we discuss the use of bacteriorhodopsin (BR), a photoactive transmembrane protein, into Fourier transform holographic associative processors. We further discuss how recent efforts to enhance the properties of the protein have improved the efficiency and longevity of these devices.

FOURIER TRANSFORM HOLOGRAPHIC ASSOCIATIVE PROCESSORS

It has long been known that human associative recall can be simulated by using a Fourier transform (FT) holographic optical loop [10-14]. Before we discuss the use of protein-based holographic films and spatial light modulators, it is useful to describe the nature of FT optical association. This introduction is important to understanding the hybrid architecture we have implemented.

Computer Simulation of the Complex Fourier Association Process

Consider two gray-scale image planes of identical pixel dimensions. Each pixel is represented by an element in a matrix of identical dimension (a 1024 × 1024 image plane is represented by a 3000 × 3000 matrix of real numbers). A smaller sample image is copied into the sample plane at an arbitrary location, and a reference image is copied into the reference plane at an arbitrary location. If we assume that an image pixel has a value from 0.0 to 1.0, where 0.0 is pure black and 1.0 is pure white, the following algorithm will yield the complex Fourier association (CFA) between the two images.

Both images are Fourier transformed by using standard two-dimensional complex FT procedures. Our implementation is an internal function of MathScriptor 2.2.16, which is freely available from www.mathscriptor.org. The FT of the single matrix, representing the sample plane (onto which the sample image is imposed), is represented by a matrix, Ψ^a, of cosine (real) components and sine (imaginary) components. We represent these elements as c_{ij}^a and s_{ij}^a, respectively. Similarly, the FT of the reference matrix yields Ψ^b, with real and imaginary components, c_{ij}^b and s_{ij}^b. The CFA of these two image planes is calculated by using the following equation:

$$\left\langle \Psi^a \left| \mathrm{A} \right| \Psi^b \right\rangle = \frac{2\left\langle \Psi^a \left| \mathrm{a} \right| \Psi^b \right\rangle}{\left|\Psi^a\right|^2 + \left|\Psi^b\right|^2} \tag{1}$$

where

$$\left|\Psi^a\right|^2 = \sum_i \sum_j \left[\left(c_{ij}^a\right)^2 + \left(s_{ij}^a\right)^2 \right]^2, \tag{2}$$

$$\left|\Psi^b\right|^2 = \sum_i \sum_j \left[\left(c_{ij}^b\right)^2 + \left(s_{ij}^b\right)^2 \right]^2, \tag{3}$$

and $$\left\langle \Psi^a \left| \mathrm{a} \right| \Psi^b \right\rangle = \sum_i \sum_j \left[\left(c_{ij}^a c_{ij}^b\right)^2 + \left(s_{ij}^a c_{ij}^b\right)^2 + \left(c_{ij}^a s_{ij}^b\right)^2 + \left(s_{ij}^a s_{ij}^b\right)^2 \right]. \tag{4}$$

The speed of the above algorithm is limited primarily by the time required to carry out a pair of two-dimensional complex Fourier transformations. High-resolution CFA on 3000 x 3000 images can take many seconds on array processors designed for the task, and thus, optical implementations are of value for real world applications. The key advantage of the above algorithm is two-fold: it allows us to explore the association process with digital precision and it reflects the same behavior as the optical associative memory that we explore below.

Translational Invariance

There are three variables that determine the relationship of a sample image with respect to a reference image: translation, rotation and size. If the sample and reference images are identical, the above equations calculate perfect association ($\left\langle \Psi^a \middle| A \middle| \Psi^b \right\rangle = 1$) regardless of where the images are located on the sample and reference planes. Thus, CFA is translationally invariant in the mathematical domain. This observation is not necessarily true in the optical domain, but in our implementation, translational invariance is retained (see below).

Rotational Variance

Consider solid white rectangles of identical width and a variable aspect ratio, in which the aspect ratio equals the ratio of the long axis to the short axis. If we associate two identical rectangles that differ only in terms of rotation, we find that the CFA varies dramatically depending upon the relative angle of the sample and reference rectangles. The results are presented in Figure 1 for rectangles of aspect ratio 1 (squares) to 10 (rectangles of length 10 by 1). Thus, we are calculating the CFA (Equation 1) for two identical objects which have a relative rotation from 0° to 90°. The CFA value is invariant to the absolute rotation of the samples, but very sensitive to the relative rotation. Higher aspect ratios lead to a more severe drop-off in CFA with relative rotation (Figure 1).

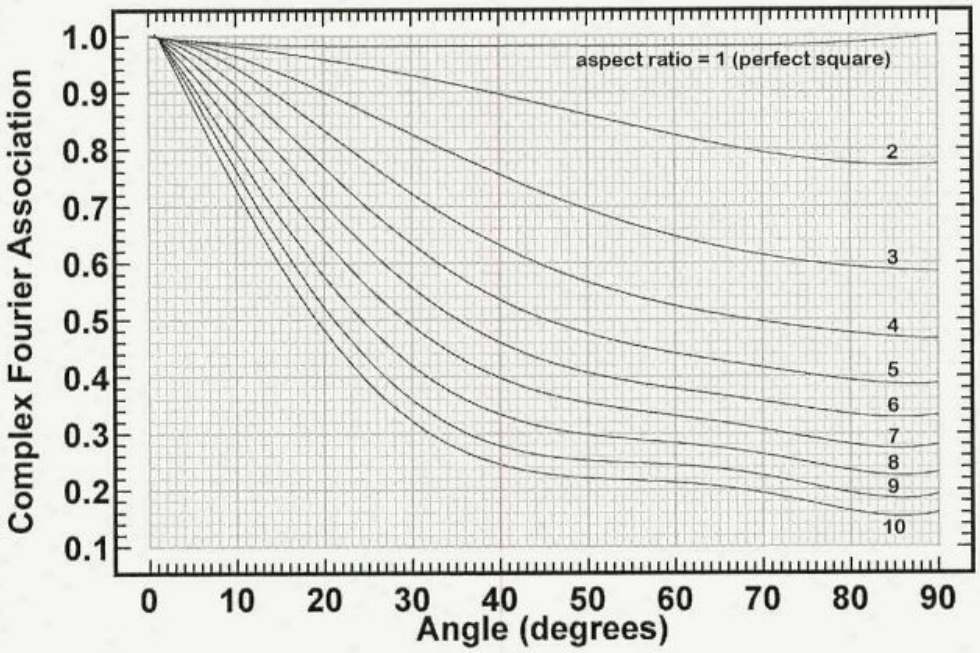

FIGURE 1

Complex Fourier association (CFA) is rotationally variant. The above graph displays CFA values for pairs of identical solid white rectangles as a function of relative angle and for various aspect ratios (= length/width). Pure squares (aspect ratio=1) show only minor dependence on angle. Rectangles with lengths ten times longer than widths (aspect ratio=10) must be aligned to within a fraction of a degree to register accurate CFA values.

Size Variance

The problem of rotational variance is compounded due to the fact that two objects must be size coordinated to properly associate in Fourier space. As shown in Figure 2, however, the nature of the objects is of minor importance to the magnitude of the variance. Figure 2 displays the CFA for a variety of identical objects, from simple letters to human faces. It is surprising how similar the size dependence of the CFA is with regards to varying objects. The nature of the size variance (Figure 2) is quite different from the shape dependence of the rotational variance (Figure 1). Thus, when an unknown object is to be characterized via Fourier association, the first step is to optimize the relative size to yield a maximal CFA. The second step is to rotate the input object to maximize the CFA. This combination works well for the vast majority of problems, although it is not uncommon to follow this cycle through two optimization passes when high discrimination is desired (i.e. size→rotation→size→rotation).

Face Identification

The human brain is remarkably adept at facial recognition. The neural processes have been studied extensively [15], but the complex architecture of the

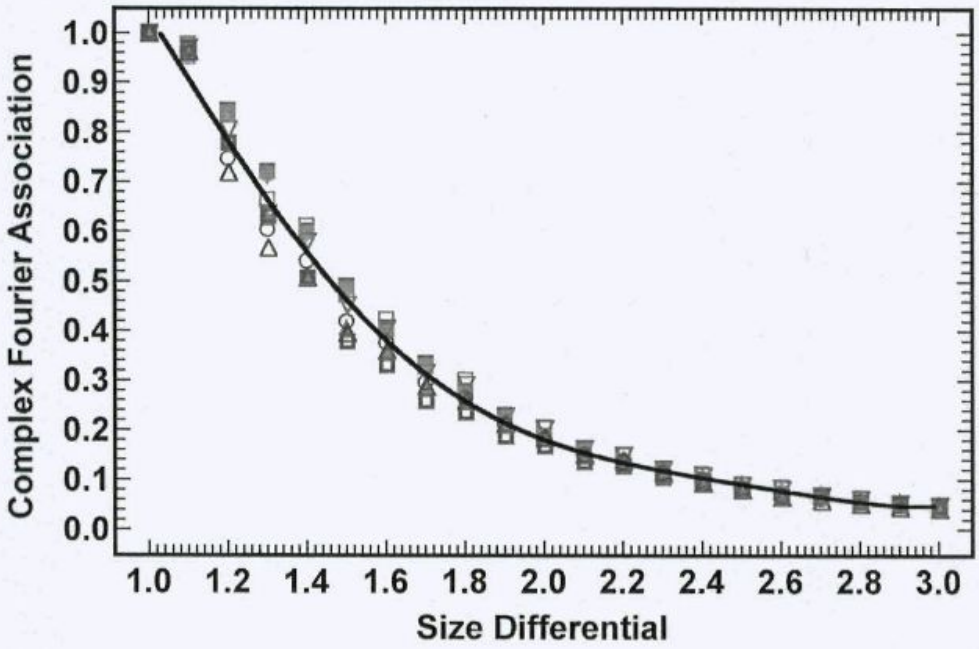

FIGURE 2

Complex Fourier association (CFA) requires that the two objects being compared have relative sizes that are shifted to an identical extent from the actual sizes of the objects. The above graph displays the CFA values for a set of identical objects, where the sample size has been changed relative to the reference size by a value of 1 (identical sizes) to 3 (sample image is three times larger than the reference image). Objects ranged from simple letters to complex objects, including human faces. Regardless of object complexity, the CFA varies with size differential by a similar magnitude.

human brain is too unique to provide useful templates for computer-based face recognition [16, 17]. Given the observation that FT optical associative memories mimic human memory recall (see above), it is appropriate to test the ability of CFA to differentiate human faces. A simple example based on four faces is presented in Figure 3. The two faces in the top quadrants are from different individuals. The two faces in the bottom quadrants are of the same individual, but differ in expression. Despite the different expressions, CFA yields a very high correlation between both faces (see Figure 4).

An important observation is that while CFA does a remarkably good job of differentiating faces, the process requires four digits of precision. In com-

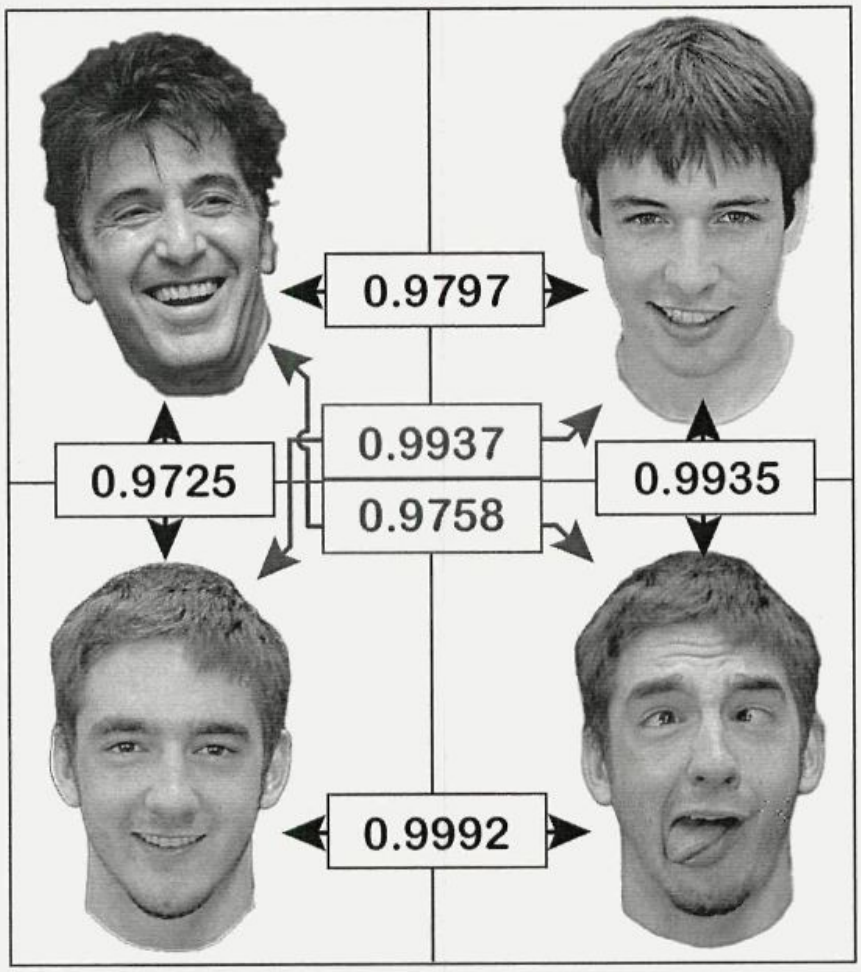

FIGURE 3
Comparison of four faces based on complex Fourier association (CFA). Each pair of faces are angle and size tuned to yield the listed maximal CFA value, which is displayed between all pairs as indicated by the arrows. Note that the bottom two faces belong to the same person, but differ significantly in expression. Nevertheless, the CFA value of 0.9992 indicates that a holographic associative memory would recognize that both images were associated with the same person. A key observation of this study is that facial recognition via CFA is accurate, but requires at least 3.5 significant digits of precision. This is an easy goal for a computer, but a non-trivial requirement for optical Fourier instrumentation.

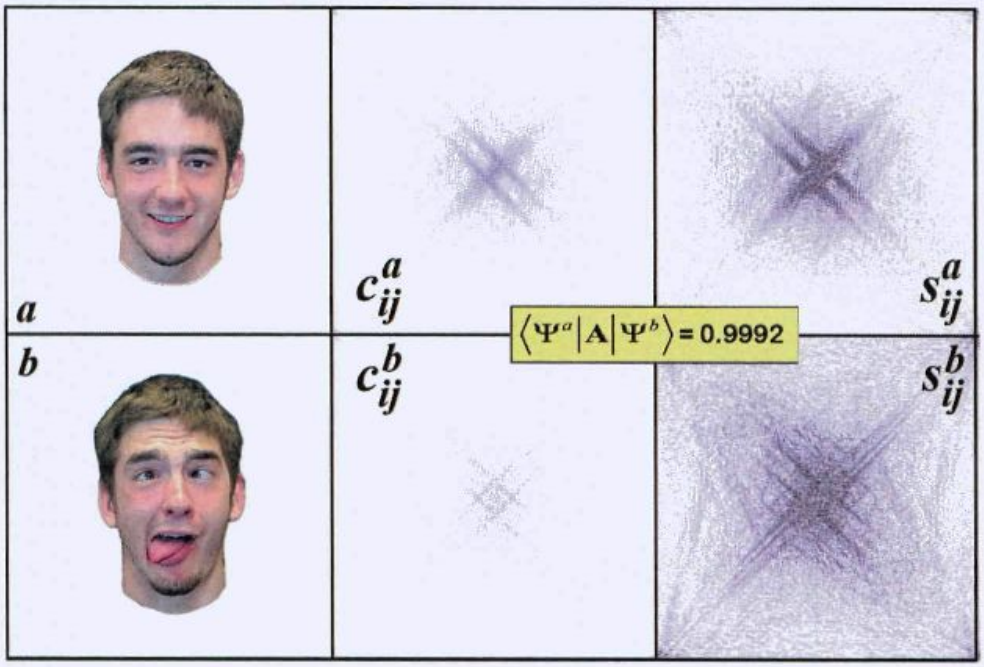

FIGURE 4
The remarkable ability of complex Fourier association (CFA) to recognize that two faces, with very different expressions, belong to the same individual. The complex Fourier transform of image a generates a cosine (c_{ij}^{a}) and a sine (s_{ij}^{a}) matrix, which are shown in the top three panels from left to right. The bottom three panels show the corresponding information for image b. The values of the matrix elements are represented by pixel darkness with white=0.0 and relative magnitude being represented by darkness of the pixel. While the two complex transforms have significantly different cosine and sine matrices, the CFA calculated using Equation 1 is nevertheless capable of revealing a high associative correlation (0.9992). The key disadvantage of CFA algorithms is the computational expense. Hence, an optical approach (Figure 5), which is thousands of times faster, is to be preferred for real-time applications.

puter terms, this is a trivial requirement. When CFA is implemented in optics, however, the equivalent of four significant digits of precision can only be achieved by using high-quality Fourier lenses and vibration-free optical platforms. We explore an optical associative processor in the next section.

Fourier Transform Optical Associative Processors

Because of the constraints associated with rotational and size variance (see above), our optical associative processor is designed using a hybrid architecture and is schematically shown in Figure 5. The main optical loop employs both feedback and thresholding and is based on the closed-loop autoassociative design of Paek and Psaltis [14]. During the write operation, reference images stored in an electronically addressable spatial light modulator [**ESLM**] are optically fed into the loop by plane wave illumination ($\lambda_w = 561$ nm) from the laser. The reference images are stored as FT holograms on thin polymer films containing BR [**H1 & H2**]. The hologram stores the reference image for approximately 10 ms before reverting to the ground state. During the readout operation, the input image (from the **ESLM** at the top of Figure 5) is continu-

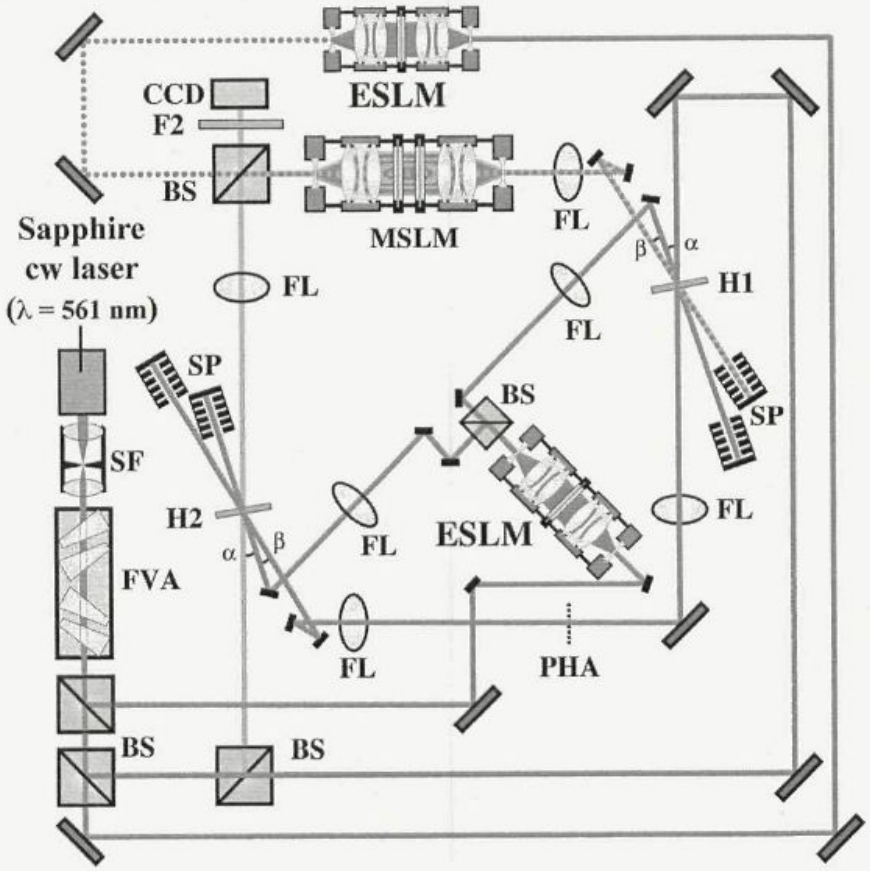

FIGURE 5
Schematic diagram of a Fourier transform holographic (FTH) associative processor with read/write FTH reference planes using thin polymer films of BR to provide real-time storage of the holograms (see text). The following symbols are used: BS (beam splitter), CCD (charge coupled device two-dimensional array), CL (condensing lens), ESLM (electronically addressable spatial light modulator), FL (Fourier lens), FVA (Fresnel variable attenuator), F1 (broadband filter for image), F2 (interference filter with transmission maximum at laser wavelength; different from λ_{max} of F1), H1 and H2 (holographic spatial light modulator), IRCO (image reduction and condensing optics), MSLM (multichannel plate spatial light modulator), PHA (pin hole array), SF (spatial filter to select TEM_{00}).

ously read into the loop. The best results are obtained by illuminating the object using plane wave illumination from the same laser. The input image beam is passed through a microchannel plate spatial light modulator [**MSLM**] operating in threshold mode. Thereafter, the Fourier transformed product of the reference image is formed and retransformed at the plane of a pinhole array [**PHA**]. The resulting correlation patterns are sampled by the pinholes (diameter ≈ 500 mm), which are precisely aligned with the optical axis of the reference images. Light from the pinhole plane is retransformed and superimposed with the reference image stored on BR hologram 2 [**H2**]. The resulting cross correlation pattern represents the superposition of all images stored on the multiplexed holograms and is fed back through the **MSLM** for another iteration. Thus, each image is weighted by the inner product between the pat-

tern recorded on the **MSLM** from the previous iteration and itself. The output locks onto the image stored in the holograms, which produces the largest correlation flux through an aligned pinhole. The optical details of the memory are described in Refs. [14, 18, 19]. Additional detail on protein-based designs can be found in Refs. [12, 13, 20, 21].

The real-time capability of the associative loop is made possible by using BR films as the transient holographic medium. The high speed of phototransformation during a write operation (<50 μs) coupled with the quick relaxation time of the **M** state (~10 ms; see below) allows for framing rates up to 100 frames/sec. Using chemically or mutationally modified forms of the protein can attain slower or faster framing rates. The write and read wavelengths of the laser source, as well as the respective angle of incidence, are chosen to optimize the diffraction efficiency of the BR films.

BACTERIORHODOPSIN

The Purple Membrane

Bacteriorhodopsin (MW = 26 kDa) is the light-transducing protein expressed in the purple membrane (PM) of the archaeon, *Halobacterium salinarum* [22-24]. This organism is native to salt marshes, which contain environments characterized by low oxygen levels and a salinity that is roughly six times greater than that of seawater. When dissolved oxygen concentrations are insufficient to support oxidative phosphorylation, BR is expressed throughout the plasma membrane of the native organism. Thus, production of metabolic energy occurs via a photosynthetic proton pumping mechanism that is coupled with the rapid synthesis of adenosine triphosphate (ATP) in the cell cytoplasm [25].

The PM, coined as such due to the presence of a distinctive purple pigment, contains a two-dimensional, semi-crystalline lattice of hexagonal subunits made up of BR trimers. The structure of BR includes a seven transmembrane, α-helical motif that is functionalized with a long-chain polyene chromophore, all-*trans* retinal, via a protonated Schiff base linkage to Lysine-216 [26]. The absorption of a single photon by the protein initiates a complex photochemical reaction, termed the BR photocycle, which is characterized by a cyclic series of conformational changes and the concurrent net translocation of a proton from the intracellular to the extracellular region (see Figure 6) [27-29]. The photocycle of native BR has a lifetime of approximately 15 ms and contains transient, spectrally distinct photointermediates that span the entire visible region of the electromagnetic spectrum. The unique photophysical properties of BR present an innate advantage for the development of photonic devices; however, the potential of this biomaterial is derived from the coupling of this photochemistry with robust structural and functional stability. In the PM, native BR has been shown to be stable at tem-

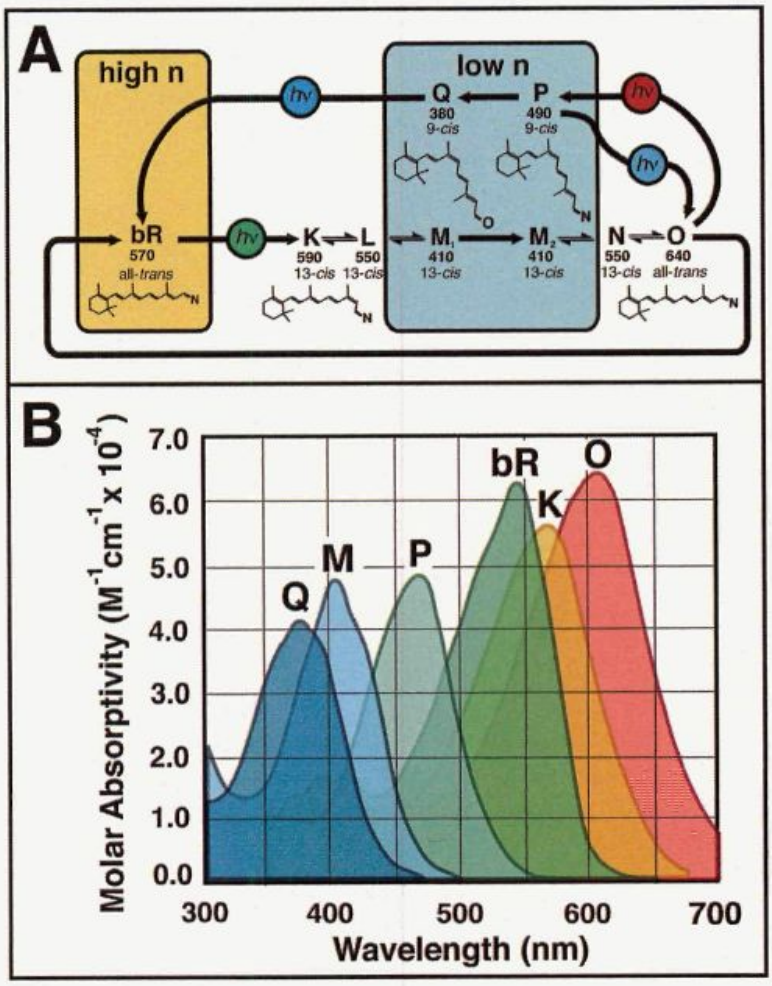

FIGURE 6
The photocycle and branched photocycle of native BR. (A) The absorption maxima (in nm) and the retinal conformation are provided below each corresponding photointermediate. The branched photocycle (the **P** and **Q** states) is reached via a sequential two-photon event, in which the protein is initially paged with an incident photon (~570 nm) and is subsequently driven by another (~640 nm) during the lifetime of the **O** state. The relative refractive index of key photointermediates are highlighted, and the absorption spectra of select photointermediates are provided in (B) (Based on Figure 2 from Ref. [20]).

peratures above 80°C [30], and, once placed in a chemically altered environment, could withstand temperatures as high as 140°C [31, 32]. In addition to thermal stability, BR exhibits high photochemical stability, which is defined as the number of times the protein can be photochemically activated before denaturing [20]. This cycling property exceeds 10^6 for BR at ambient temperature and is considerably higher than that of most photochromic organic molecules [33, 34].

The Photochromic Properties of Bacteriorhodopsin

For FT holographic associative processors, the spectral separation and the significant change in refractive index throughout the photocycle implicate the

potential for use in the architectures described above. The absorption of a photon by all-*trans* retinal potentiates the formation of a Franck Condon excited state and a near instantaneous shift of electron density down the polyene chain of the chromophore, thereby initiating an isomerization around the $C_{13}=C_{14}$ double bond to form 13-*cis* retinal (see Figure 6) [23]. This 500 fs process is referred to as the primary photochemical event of BR (**bR→K**), and is followed by a cascade of thermally driven photointermediates (**L**, **M**, **N**, **O**, and back to **bR**) [35, 36]. The **M** state forms approximately 50 μs after the absorption of a photon and is associated with the transfer of a proton from the protonated Schiff base to Aspartic acid-85, which is the residue that serves as the primary counterion in the resting state [37]. This transition results in a dramatic hypsochromic shift in the absorption maximum (λ_{max}; 570 nm → 410 nm), which has a time constant of 10 ms. For real-time holographic associative processing, the blue light absorbing **M** state is the secondary constituent in the **bR/M** photochromic pair. In addition to the thermal decay pathway of the **M** state back to the resting state, the **bR** state can also be regenerated from the **M** state through the absorption of blue light. This photoreversibility is described using the following equation,

$$bR(\lambda_{max} = 570nm) \underset{h\nu(\Phi_2 \approx 0.65)}{\overset{h\nu(\Phi_1 \approx 0.65)}{\rightleftharpoons}} M(\lambda_{max} = 410nm) \tag{5}$$

where Φ_1 and Φ_2 are the quantum efficiencies of the forward (**bR→M**) and reverse (**M→bR**) reactions, respectively. Due to the unusually high quantum efficiencies of both reactions, BR has proven to be an ideal optical recording medium for holographic processors. However, this application relies on the manipulability of the **M** state time constant, which is prohibitively short in the native form of the protein. Norbert Hampp and colleagues have achieved success in designing a real-time holographic interferometer based on a chemically modified BR mutant, which contains a long-lived **M** intermediate that persists on the order of seconds [38-40]. Despite this success, a system with pure photoswitching without a transient thermal decay has yet to be realized using the **M** state, thereby preventing applications in long-term data storage. Since the advent of this device, however, a long-term photoproduct of BR (the **Q** state) has been discovered and exploited to form a new prospect of photochromic equilibrium with two long-lived states.

A branching reaction of the main photocycle is accessed via a sequential two-photon event. The photocycle is first initiated through light absorption by the chromophore, and the branching reaction is obtained through the subsequent exposure to red light (~640 nm) while the protein is in the **O** state [41]. The **P** state, which contains a 9-*cis* chromophore and a λ_{max} of 490 nm, is the direct photochemical intermediate of this reaction pathway, and is followed by the hydrolysis of 9-*cis* retinal and the formation of the **Q** state (λ_{max} = 380 nm) [41, 42]. The **Q** state photoproduct is thermally stable for several years

(requiring 190 kJ mol^{-1} to initiate a reversion) and may be converted back to the **bR** resting state upon the absorption of a high-energy photon (~380 nm). The discovery of the branched photocycle of BR has yielded advances in the development of sequential two-photon volumetric memories based on the protein, where two stable products (**bR** and **Q**) are assigned to binary bit 0 and binary bit 1, respectively [20].

The stability of this photoproduct and the ability to probe and manipulate the protein medium via differential absorptivity has lead to a dramatic increase of potential in biomolecular devices. The architectural requirements of the sequential two-photon stimulus parameters of BR in the PM are more suitable for three-dimensional memories [20], and not for the FT holographic associative memories described here. Alternatively, a blue-shifted species analogous to the **P** and **Q** states can be exploited in the blue membrane (BM) form of the protein, in which the PM is transformed into a biphasic photochromic material capable of long-lived changes in the refractive index.

The Blue Membrane

The formation of the BM occurs through altering the electrostatic interaction of retinal with key residues using either chemical or mutational modification of the protein. Native BR contains 4 moles of calcium(II) and magnesium(II) per mole of protein at pH 6.0 [43, 44], and the removal of these cations perturbs the retinal binding pocket, inducing a reversible color change from purple ($\lambda_{max} = 570$ nm) to blue ($\lambda_{max} = 605$ nm) [44-48]. Cation displacement is accomplished by either acidification of the PM [46, 49, 50] or through deionization methods at standard pH [43, 45, 50-52]. Despite the efficiency of these methods, both forms of chemical modification result in a destabilized form of the protein [53, 54]. Mutational manipulation has proven to be effective at inducing localized changes to create a stable form of the BM. Amino acids that stabilize the protonated Schiff base are often targeted for mutagenesis [55, 56], and these mutants have been successfully implemented into long-term holographic memory devices [57, 58].

Within the BM, the chromophore exists in both the all-*trans* and 13-*cis* conformations in the resting state ($\lambda_{max} = 605$ nm) [49, 59]. The primary photochemical event (all-*trans* $\rightarrow$ 13-*cis*) is still initiated upon the absorption of a photon, however, the reaction has a much lower efficiency ($\Phi \approx 0.10$) and contains a truncated photocycle that does not terminate with the net translocation of a proton [60]. Despite these altered photophysical characteristics, the BM is capable of forming blue-shifted intermediates that are similar to the **P** and **Q** states of the branched photocycle. Under sustained illumination with red light (~640 nm), a reversible photoconversion is initiated to form a species with a λ_{max} of 490 nm, which is often referred to as the pink membrane [59]. The pink membrane is characterized by the 9-*cis* conformation of retinal and is a long-lasting photoproduct of the BM form of BR, which can only be reverted back to the BM resting state (**bR**) via blue light (~400 nm) illumina-

tion [49, 50]. The pink membrane has been shown to form two thermal decay products (λ_{max} = 450 nm and 380 nm), the latter of which is characterized by a hydrolyzed 9-*cis* retinal (**Q** state) [41,51,52,61]. In application, blue←→pink photochromism is isolated in dehydrated polymer films [52, 62].

The application that includes the blue/pink photochromic pair differs in two ways from the **bR/M** pair. First, the pink membrane form is stable for weeks or months in contrast with the transient intermediates of the BR photocycle [52]. Secondly, the quantum efficiencies of the forward and back reactions are minute compared to the reactions of the PM [59]. The low sensitivity to incident light, however, is of little consequence and can even be advantageous. Low quantum efficiencies signify that thin films would be stable under ambient light conditions, which would elicit transferrable long-term holograms for data storage. Moreover, under write and read conditions, the low efficiency is circumvented due to the widespread availability of high-energy diode lasers.

HOLOGRAPHIC PROPERTIES OF BACTERIORHODOPSIN THIN FILMS

Bunkin and coworkers were the first to propose the use of BR in protein-based thin films as a holographic storage medium [63]. Bacteriorhodopsin has since been characterized as an efficient holographic material that exhibits significant potential in pattern recognition, optical filtering, and artificial neural networking [13, 34, 38, 64-67]. Protein-based thin films are prepared by using an optically transparent polymer or polymer blend base to immobilize the PM (or BM), thereby creating ordered protein-polymer assemblies. The thin films are tunable through the manipulation of concentration and chemical environment, genetic engineering, and read/write laser intensity, and have a resolution that is more than 5000 lines/mm [67]. Below, we discuss the holographic properties that enable BR-based thin films to be applied in associative memories.

Holographic Properties

Figure 7 provides a theoretical schematic describing the optical design necessary to record plane wave holograms onto a thin protein film and to read the resulting spatial light intensity distribution. This architecture is capable of recording volume transmission holograms, where the object and reference beams approach the recording medium from the same side of the film. Data recording is initiated using two identical laser beams that are derived from the same source and have a wavelength that couples sufficiently with the λ_{max} of BR (~570 nm). The two incident beams overlap at the plane of the film and are polarized perpendicular to the plane of incidence to make an angle (ϕ_w) with respect to the film normal. As a result of the coherence properties of

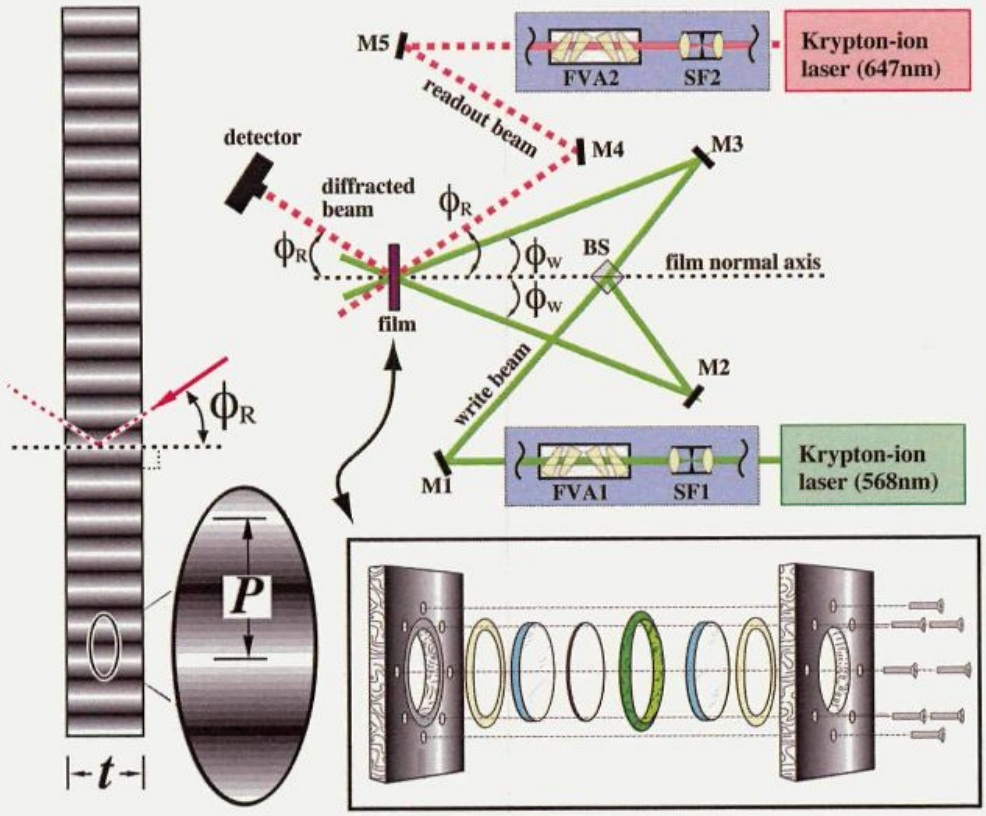

FIGURE 7
A schematic representation of the experimental set up used in writing and reading a volume transmission hologram. The volume transmission hologram (left) is representative of a BR-based thin film, wherein the dark and light lines represent regions of high (**bR**) and low (**M**) refractive index, respectively (see text). A BR hologram is written by overlapping beams derived from the same laser, and the hologram is non-destructively read using a probing beam at the Bragg angle (ϕ_R). See the text for further details on holographic properties.The inset depicts the general architecture of the formation of the BR-based thin film used in experiment. The following symbols are used: P (fringe spacing), t (film thickness), ϕ_W (writing beam angle), FVA (Fresnel variable attenuator), BS (beamsplitter), SF (spatial filter), M (mirror).

emitted laser light, a three-dimensional interference pattern is recorded onto the film, which has a thickness (t) that is significantly greater than the recorded interference pattern induced by laser light. The periodic spatial light intensity distribution presented in Figure 7 can also be described mathematically in one dimension by

$$I(x) = (I_1 + I_2)\left[1 + V\cos\frac{2\pi x}{P}\right] \tag{6}$$

where I_1 and I_2 are the intensities of the individual beams, V is the contrast ratio of the interference pattern given by

$$V = \frac{2(I_1 I_2)^{1/2}}{(I_1 + I_2)}, \tag{7}$$

and P is the fringe spacing of the grating (see Figure 7), which can be calculated using

$$P = \frac{\lambda_w}{2 \sin \phi_w}. \tag{8}$$

In real-time holographic applications, the interference pattern can be defined as a periodic spatial concentration distribution of the **bR** and **M** states. The film is a recording of phase and amplitude information of the incident laser light and can be viewed as a spatial modulation of the absorption coefficients and the indices of refraction. In places of constructive interference, **bR** is driven to the **M** state and the associated volume has a lower refractive index than initially observed. Conversely, destructive interference does not initiate the photochemical reaction of BR and the relevant volumes remain in **bR** state, which has a relatively high refractive index. An accurate description of the relationship between absorption and refraction of a modulated BR thin film is achieved through the use of the Kramers-Kronig (KK) transformation [68].

Application of the Kramers-Kronig Transformation

As light passes through any optically transparent medium, the material will absorb some portion of that incident light. The relationship between absorption and index of refraction (n) is fundamental to the diffraction or reconstruction processes in holographic processing applications. Thus, complex indices of refraction must be applied to accurately describe the behavior of these materials, using both real (n) and imaginary (κ) terms to indicate phase speed and loss of absorption, respectively [12]. These two terms are measured and correlated via the KK transformation [68]. The KK relation analyzes the complex index of refraction using the following integral relation:

$$\mathrm{n}(\omega) - \mathrm{n}(\omega_\infty) = \frac{2}{\pi} \mathrm{P.V.} \int_0^\infty \frac{\omega' \kappa(\omega') \mathrm{d}\omega'}{\omega'^2 - \omega^2}, , \tag{9}$$

where κ is the absorption index, ω is the angular frequency, and P.V. is the Cauchy principal value of the succeeding improper integral. The absorption index can be related to the absorption coefficient using

$$\kappa = \frac{\alpha \mathrm{c}}{2\omega'}, \tag{10}$$

where α is the absorption coefficient in wavenumbers (cm^{-1}) and c is the speed of light in the centimeter-gram-second (CGS) system of units. The absorption coefficient can be linked to experimentally measured absorbance of the film by using the following equation:

$$\alpha(\lambda') = 2.3026 \frac{\mathrm{A}(\lambda')}{t}, \tag{11}$$

where t is the thickness of the sample under investigation. Experimental absorbance can then be incorporated into Equation 9 to produce the following relationship:

$$n(\omega) - n(\omega_\infty) = \frac{2.3026}{2\pi^2 t} \text{P.V.} \int_0^\infty \frac{A(\lambda')d\lambda'}{1 - \frac{\lambda'^2}{\lambda^2}}. \quad (12)$$

Subsequently, this equation can be modified to include the specific photochemical conversion of interest, particularly the **bR→M** conversion observed in the transient BR photocycle or the formation of the pink membrane from the BM:

$$\Delta n(\lambda) = \frac{2.3026}{2\pi^2 t} \text{P.V.} \int_0^\infty \frac{A_X(\lambda') - A_{bR}(\lambda')d\lambda'}{1 - \frac{\lambda'^2}{\lambda^2}}. \quad (13)$$

Here, X refers to either the **M** or pink membrane states and **bR** refers to the resting state of native BR or of the BM. Figure 8 exhibits the overall change in refractive index of BR through a KK analysis of both the real-time computing (Figure 8, top) and long-term data storage (Figure 8, bottom) applications. Despite differences in total holographic efficiency, the **bR/M** (6.6%) and blue/pink (2.4%) photochromic pairs would be incorporated into separate architectural systems that are optimized for specific holographic properties and applications.

Analysis of Diffraction Efficiency

The analysis of photodiffractive properties of volume transmission holograms has been established through Kogelnik's coupled wave theory [69]. Spatial modulations of the absorption coefficient and the index of refraction of BR thin films are described using the following truncated Fourier expansions [69, 70]:

$$a(x) = a_{avg} + a_1 \cos(2\pi x / P), \quad (14)$$

$$n(x) = n_{avg} + n_1 \cos(2\pi x / P), \quad (15)$$

where $\alpha(x)$ and $n(x)$ are spatial dependent values, a_{avg} and n_{avg} are the average values, and a_1 and n_1 are the modulation amplitudes, all with respect to the absorption coefficient (α) and the index of refraction (n). These parameters contribute to the total diffraction of the system, with the absorption coefficient related to absorptive modulation and the index of refraction related to the phase (optical path) modulation of the light electric field amplitude.

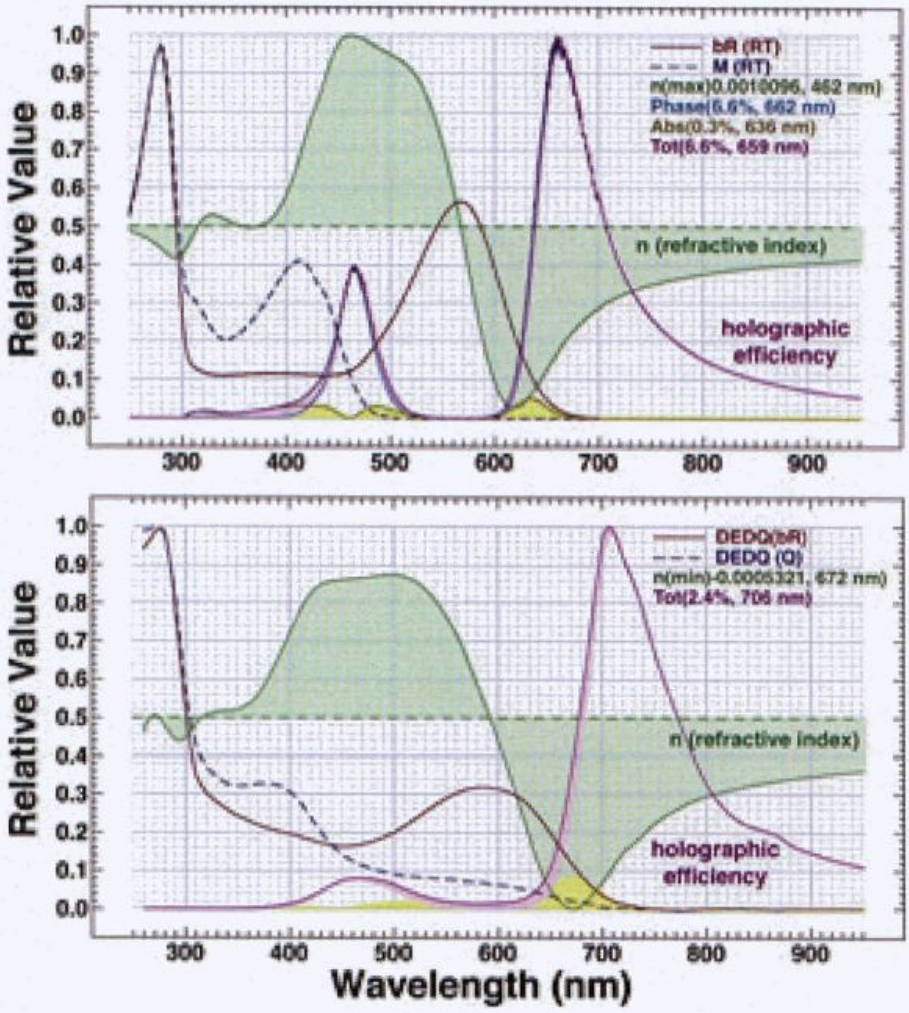

FIGURE 8

A Kramers–Kronig analysis of wavelength dependence of the diffraction efficiency associated with the **bR/M** photochromic pair used in real-time (RT) associative processing (top) and the **bR/Q** pair of the BR mutant, D85E/D96Q (DEDQ), as a representation of the blue/pink transition (bottom). See the text for a description of the calculations.

The diffraction efficiency of a hologram stored in a BR thin film can be defined as the ratio of the diffracted light intensity, I_D, to the intensity of the reading beam, I_0. In a similar manner to the KK transformation, the diffraction efficiency has both an absorptive and a refractive component and can be explained using the following equations [12]:

$$\eta_{\text{total}} = \frac{I_D}{I_0} = \eta_{\text{abs}} + \eta_{\text{phase}}, \tag{16}$$

$$\eta_{\text{abs}} = D^2 \sinh^2 \left\{ \frac{\Delta\alpha(\lambda_r)t}{2\cos\phi_r} \right\} \tag{17}$$

$$\eta_{phase} = D^2 \sin^2 \left\{ \frac{\pi \Delta n(\lambda_r) t}{\lambda_r \cos \phi_r} \right\} \tag{18}$$

$$D = \exp \left\{ \frac{-\alpha_{ave}(\lambda_r) t}{\cos \phi_r} \right\} \tag{19}$$

where η_{total} is the total diffraction efficiency, η_{abs} is the diffraction efficiency due to absorption, η_{phase} is the diffraction efficiency due to refraction, t is the thickness of the film, λ_r is the wavelength of the read laser, and ϕ_r is the angle of incidence of the read laser. The read angle, ϕ_r, is an experimentally derived measurement that can be adjusted as needed, however, the optimal angle to achieve maximum efficiency can be found by using the Bragg condition:

$$\phi_r = \sin^{-1} \left\{ \frac{\lambda_r \sin \phi_w}{\lambda_w} \right\} \tag{20}$$

where ϕ_w is the angle of the write beam relative to the film normal and λ_w is the wavelength of the write beam. The a and n terms in Equations 17 to 19 are related to the modulation amplitudes of the absorptive and refractive terms, respectively. The D term in the above equations is a measure of the amplitude of the spatial modulation and is included to restrict the maximum value of the absorptive component of the calculated total diffraction efficiency. This term requires that there is no spatial modulation of the refractive index, only modulation of the absorption constant. An upper limit for the amplitude of the sinusoidal modulation must be present, whereas the absorption modulation at the read wavelength is less than or equal to the average absorption. Thus, the highest diffraction efficiency for an absorption grating is of $\eta_{abs} = 3.7\%$, which represents the case in which $a_1(\lambda_R)$ is equal to $a_{avg}(\lambda_R)$ [69]. The η_{phase} term is entirely determined by the change of refractive index and can have diffraction efficiencies that approach 100% [12]. Therefore, devices that require diffraction efficiencies of 3.7% or higher must use phase holograms or mixed absorption and phase holograms.

GENETIC OPTIMIZATION OF BACTERIORHODOPSIN

Although nature has yielded a robust photoactive protein, protein engineering of native BR is a necessary step for use as the primary photochromic material in devices. Manipulation of the kinetics and quantum efficiencies of the photointermediates of the BR photocycle are the primary focus of optimization, and mutagenesis of the **M** and **Q** states are particularly critical for holographic processors. Because the **M** state is transient, dynamic hologra-

phy utilizing the **bR/M** photochromic pair is limited to the time constant of this transition. In order to improve or lengthen the lifetime of the **M** state, amino acids involved in proton transfer to the Schiff base are targeted for mutagenesis [34, 39, 71, 72]. Devices based on the **Q** state remove the factor of time sensitivity due to the isolation of a stable photoproduct [42]. Because the **Q** state does not exist in nature, the genetic enhancement of the formation and reversion efficiencies are of interest for long-term data storage [72]. Mutagenesis has been effective at enhancing the formation of the BM through manipulation of the primary counterion to the protonated Schiff base [55, 56].

Directed evolution (DE) provides a cost-effective and time efficient method for genetically optimizing biological macromolecules, specifically BR, to serve in non-native environments [71-73]. This process enhances a protein toward a specific characteristic via repeated iterations of genetic mutation, screening, and differential selection. Historically, DE has been used to modify properties of enzymes for pharmaceutical and industrial applications [74-78]. Protein redesign of BR by DE is accomplished through an iterative combination of site-directed, site-specific saturation, semi-random and random mutagenesis. Site-directed mutagenesis (SDM) targets a single amino acid that plays a key role in the structure or function of BR and exchanges it with an alternate amino acid. Semi-random mutagenesis (SRM) and random mutagenesis (RM) will produce a large number of indiscriminate mutants by using doped oligonucleotides or by exploiting the error prone nature of polymerase chain reaction (PCR). Site-specific saturation mutagenesis (SSSM) is a process that combines SDM and SRM and allows for the characterization of protein mutants containing multiple amino acid substitutions via the saturation of a key residue at a specific locus on the bacterioopsin (*bop*) gene. The observable nature of the photochemical properties of BR facilitates the automated screening and characterization of microgram quantities of mutants, which has resulted in the identification of mutants that outperform the native protein. Thus, properties such as **M** state lifetime or **Q** state formation can be monitored and optimized over several stages of DE for specific use in biomolecular devices.

CONCLUSIONS

Bacteriorhodopsin continues to serve as the archetypal biomaterial for investigations involving optical processing. This protein combines dynamic photochromism with high quantum efficiencies, significant changes in refractive index, and high structural stability. Here, we have examined several aspects of CFA and explored how these algorithms can be implemented using BR-based thin films. The architectures described here have been successfully implemented into prototypes involving both real-time computing and long-

term data storage. Until recently, the inherent limitations of the native protein have prevented commercial development. However, advancements in genetic engineering and DE have circumvented many of these limitations and have once again stimulated interest in creating optical associative processors based on BR. We anticipate that the first step towards fully realizing these goals relies on the incorporation of optical and biomolecular architectures into hybrid semiconductor-based systems. The advantages of using biological materials in computing architectures will continue to drive the development and optimization of these devices, and will challenge computer scientists to reinvestigate protein-based architectures in the development of artificial intelligence.

ACKNOWLEDGEMENTS

This research was funded in part by grants to RRB from the National Science Foundation (EMT-0829916) and the Harold S. Schwenk Sr. Distinguished Chair in Chemistry.

NOMENCLATURE

RAM	Random-access memory
CAM	Content-addressable memory
BR	Bacteriorhodopsin
FT	Fourier transform
CFA	Complex Fourier association
Ψ^a	Matrix representing a sample plane
c_{ij}^a	Cosine (real) component of Ψ^a
s_{ij}^a	Sine (imaginary) component of Ψ^a
Ψ^b	Matrix representing a reference plane
c_{ij}^b	Cosine (real) component of Ψ^b
s_{ij}^b	Sine (imaginary) component of Ψ^b
ESLM	Electronically addressable spatial light modulator
H1	Bacteriorhodopsin hologram 1
H2	Bacteriorhodopsin hologram 2
MSLM	Microchannel plate spatial light modulator
PHA	Pinhole array
PM	Purple membrane
ATP	Adenosine triphosphate
BM	Blue membrane
Φ	Quantum efficiency
λ_{max}	Absorption maximum

ϕ_w	Write laser angle
λ_w	Write laser wavelength
t	Thickness
I_1	Intensity of beam 1
I_2	Intensity of beam 2
V	Contrast ratio of interference pattern
P	Fringe spacing of the grating
KK	Kramers-Kronig
n	Refractive index
κ	Absorption index
ω	Angular frequency
P.V.	Cauchy principal
α	Absorption coefficient
$\alpha(x)$	Spatial dependent value of the absorption coefficient
$n(x)$	Spatial dependent value of the index of refraction
a_{avg}	Average value of the absorption coefficient
n_{avg}	Average value of the index of refraction
a_1	Modulation amplitude of the absorption coefficient
n_1	Modulation amplitude of the index of refraction
I_D	Diffracted light intensity
I_0	Reading beam intensity
η_{total}	Total diffraction efficiency
η_{abs}	Diffraction efficiency due to absorption
η_{phase}	Diffraction efficiency due to refraction
λ_r	Read laser wavelength
ϕ_r	Read laser angle
D	Spatial modulation amplitude
DE	Directed evolution
SDM	Site-directed mutagenesis
SRM	Semi-random mutagenesis
RM	Random mutagenesis
PCR	Polymerase chain reaction
SSSM	Site-specific saturation mutagenesis
bop	bacterio-opsin

REFERENCES

[1] Reijmers, L.G., Perkins, B.L., Matsuo, N., Mayford, M. (2007). Localization of a stable neural correlate of associative memory. *Science* **317**, 1230–1233.

[2] Mayes, A., Montaldi, D., Migo, E. (2007). Associative memory and the medial temporal lobes. *Trends Cognit. Sci.* **11**, 126–135.

[3] Cutsuridis, V., Cobb, S., Graham, B.P. (2010). Encoding and retrieval in a model of the hippocampal CA1 microcircuit. *Hippocampus* **20**, 423–446.

[4] Cutsuridis, V. , Wennekers, T. (2009). Hippocampus, microcircuits and associative memory. *Neural Netw.* **22**, 1120–1128.

[5] Abu-Mostafa, Y.S. , Psaltis, D. (1987). Optical Neural Computers. *Sci. Am.* **256**, 88–95.
[6] Moore, G. (1965). Cramming more components onto integrated circuits. *Electronics* **38**, 114–117.
[7] Horowitz, M., Alon, E., Patil, D., Naffziger, S., Kumar, R., Bernstein, K. (2005) *Scaling, power, and the future of CMOS.* Electronic Devices Meeting, December 5, 2005, Washington, D.C., USA.
[8] Esmaeilzadeh, H., Blem, E., St. Amant, R., Sankaralingam, K., Burger, D. (2011) *Dark Silicon and the End of Multicore Scaling*. Proceedings of the 38th International Symposium on Computer Architecture, June 4-8, 2011, San Jose, California, USA.
[9] Greco, J.A., Wagner, N.L., Ranaghan, M.J., Rajasekaran, S., Birge, R.R. (2012) Biomolecular Electronics and Protein-Based Optical Computing. In: Katz, E. (Ed.), *Biomolecular Information Processing: From Logic Systems to Smart Sensors and Actuators*, Wiley-VCH, Weinheim, Germany. pp. 33–59.
[10] Psaltis, D., Park, C.H., Jong, J. (1988). Higher order associative memories and their optical implementations. *Neural Netw.* **1**, 149–163.
[11] Soffer, B.H., Dunning, G., Owechko, Y., Marom, E. (1986). Associative holographic memory with feedback using phase-conjugate mirrors. *Opt. Lett.* **11**, 118–120.
[12] Gross, R.B., Izgi, K.C., Birge, R.R. (1992). Holographic thin films, spatial light modulators and optical associative memories based on bacteriorhodopsin. *Proc. SPIE* **1662**, 186–196.
[13] Birge, R.R., Fleitz, P.A., Gross, R.B., Izgi, J.C., Lawrence, A.F., Stuart, J.A., Tallent, J.R. (1990). Spatial light modulators and optical associative memories based on bacteriorhodopsin. *Proc. IEEE EMBS* **12**, 1788–1789.
[14] Paek, E.G. , Psaltis, D. (1987). Optical associative memory using Fourier transform holograms. *Opt. Eng.* **26**, 428–433.
[15] Haxby, J.V., Hoffman, E.A., Gobbini, M.I. (2002). Human neural systems for face recognition and social communication. *Biol. Psychiatry* **51**, 59–67.
[16] Zhao, W., Chellappa, R., Phillips, P.J., Rosenfeld, A. (2003). Face recognition: A literature survey. *ACM Computing Surveys (CSUR)* **35**, 399–458.
[17] Turk, M.A., Pentland, A.P. (1991). *Face recognition using eigenfaces*. Proc. IEEE Conf. on Computer Vision and Pattern Recognition, pp. 586–591.
[18] Paek, E.G., Jung, E.C. (1991). Simplified holographic associative memory using enhanced nonlinear processing with thermoplastic plate. *Opt. Lett.* **16**, 1034–1036.
[19] Paek, E.G., Jung, E.C., Silberberg, Y., Ravi, T.S. (1991). Enhanced nonlinear recording using a thermoplastic plate. *Appl. Phys. Lett.* **59**, 1019–1021.
[20] Birge, R.R., Gillespie, N.B., Izaguirre, E.W., Kusnetzow, A., Lawrence, A.F., Singh, D., Song, Q.W., Schmidt, E., Stuart, J.A., Seetharaman, S., Wise, K.J. (1999). Biomolecular electronics: Protein-based associative processors and volumetric memories. *J. Phys. Chem. B.* **103**, 10746–10766.
[21] Rajasekaran, S., Kundeti, V., Birge, R., Kumar, V., Sahni, S. (2011). Efficient Algorithms for Computing With Protein-Based Volumetric Memory Processors. *IEEE Trans. Nanotech.* **10**, 881-890.
[22] Oesterhelt, D. , Stoeckenius, W. (1971). Rhodopsin-like Protein from the purple membrane of *Halobacterium halobium. Nature* **233**, 149–152.
[23] Birge, R.R. (1990). Nature of the primary photochemical events in rhodopsin and bacteriorhodopsin. *Biochim. Biophys. Acta* **1016**, 293–327.
[24] Lanyi, J.K. (2004). Bacteriorhodopsin. *Annu. Rev. Physiol.* **66**, 665–688.
[25] Oesterhelt, D., Stoeckenius, W. (1973). Functions of a new photoreceptor membrane. *Proc. Natl. Acad. Sci. USA* **70**, 2853–2857.
[26] Luecke, H., Schobert, B., Richter, H.-T., Cartailler, J.-P., Lanyi, J.K. (1999). Structure of bacteriorhodopsin at 1.55 Å resolution. *J. Mol. Biol.* **291**, 899–911.
[27] Stuart, J.A. , Birge, R.R. (1996). Characterization of the primary photochemical events in bacteriorhodopsin and rhodopsin. In: Lee, A.G. (Ed.), *Biomembranes*, JAI Press: London, England. pp. 33-140.

[28] Zimányi, L., Váró, G., Chang, B., Ni, B., Needleman, R., Lanyi, J. (1992). Pathways of proton release in the bacteriorhodopsin photocycle. *Biochemistry* **31**, 8535–8543.

[29] Balashov, S.P. (2000). Protonation reactions and their coupling in bacteriorhodopsin. *Biochim. Biophys. Acta* **1460**, 75–94.

[30] Jackson, M.B., Sturtevant, J.M. (1978). Phase Transitions of the Purple Membranes of *Halobacterium halobium*. *Biochemistry* **17**, 911–915.

[31] Shen, Y., Safinya, C.R., Liang, K.S., Ruppert, A.F., Rothschild, K.J. (1993). Stabilization of the membrane protein bacteriorhodopsin to 140°C in two-dimensional films. *Nature* **366**, 48–50.

[32] Lukashev, E.P. , Robertson, B. (1995). Bacteriorhodopsin retains its light-induced proton-pumping function after being heated to 140°C. *Bioelectrochem. Bioenerg.* **37**, 157–160.

[33] Bräuchle, C., Hampp, N., Oesterhelt, D. (1991). Optical applications of bacteriorhodopsin and its mutated variants. *Adv. Mater.* **3**, 420–428.

[34] Hampp, N., Bräuchle, C., Oesterhelt, D. (1990). Bacteriorhodopsin wildtype and variant aspartate-96 to asparagine as reversible holographic media. *Biophys. J.* **58**, 83–93.

[35] Nuss, M.C., Zinth, W., Kaiser, W., Kölling, E., Oesterhelt, D. (1985). Femtosecond spectroscopy of the first events of the photochemical cycle in bacteriorhodopsin. *Chem. Phys. Lett.* **117**, 1–7.

[36] Mathies, R.A., Brito Cruz, C.H., Pollard, W.T., Shank, C.V. (1988). Direct observation of the femtosecond excited-state cis-trans isomerization in bacteriorhodopsin. *Science* **240**, 777–779.

[37] Subramaniam, S., Greenhalgh, D.A., Khorana, H.G. (1992). Aspartic acid 85 in bacteriorhodopsin functions both as proton acceptor and negative counterion to the Schiff base. *J. Biol. Chem.* **267**, 25730–25733.

[38] Hampp, N., Popp, A., Bräuchle, C., Oesterhelt, D. (1992). Diffraction efficiency of bacteriorhodopsin films for holography containing bacteriorhodopsin wildtype BR_{WT} and its variants BR_{D85E} and BR_{D96N}. *J. Phys. Chem.* **96**, 4679–4685.

[39] Hampp, N., Thoma, R., Zeisel, D., Bräuchle, C., Oesterhelt, D. (1994). Bacteriorhodopsin variants for holographic pattern recognition. *Adv. Chem.* **240**, 511–526.

[40] Hampp, N. (2000). Bacteriorhodopsin: mutating a biomaterial into an optoelectronic material. *Appl. Microbiol. Biotechnol.* **53**, 633–639.

[41] Popp, A., Wolperdinger, M., Hampp, N., Bräuchle, C., Oesterhelt, D. (1993). Photochemical conversion of the O-intermediate to 9-cis-retinal-containing products in bacteriorhodopsin films. *Biophys. J.* **65**, 1449–1459.

[42] Gillespie, N.B., Wise, K.J., Ren, L., Stuart, J.A., Marcy, D.L., Hillebrecht, J., Li, Q., Ramos, L., Jordan, K., Fyvie, S., Birge, R.R. (2002). Characterization of the branched-photocycle intermediates P and Q of bacteriorhodopsin. *J. Phys. Chem. B* **106**, 13352–13361.

[43] Chang, C.-H., Jonas, R., Melchiore, S., Govindjee, R., Ebrey, T.G. (1986). Mechanism and role of divalent cation binding of bacteriorhodopsin. *Biophys. J.* **49**, 731–739.

[44] Zhang, Y.N., Sweetman, L.L., Awad, E.S., El-Sayed, M.A. (1992). Nature of the Ca^{2+} binding sites in Ca^{2+}-regenerated bacteriorhodopsin. *Biophys. J.* **61**, 1201–1206.

[45] Chang, C.-H., Jonas, R., Govindjee, R., Ebrey, T.G. (1988). Regeneration of blue and purple membranes from deionized bleached membranes. *Photochem. Photobiol.* **47**, 261–265.

[46] Kimura, Y., Ikegami, A., Stoeckenius, W. (1984). Salt and pH-dependent changes of the purple membrane absorption spectrum. *Photochem. Photobiol.* **40**, 641–646.

[47] Duñach, M., Pardós, E., Seigneuret, M., Rigaud, J. (1988). On the molecular mechanism of the blue to purple transition of bacteriorhodopsin. UV-difference spectroscopy and electron spin resonance studies. *J. Biol. Chem.* **263**, 7555–7559.

[48] Jonas, R., Ebrey, T.G. (1991). Binding of a single divalent cation directly correlates with the blue-to-purple transition in bacteriorhodopsin. *Proc. Natl. Acad. Sci. U.S.A.* **88**, 149–153.

[49] Maeda, A., Tatsuo, I., Yoshizawa, T. (1981). Photoreaction of the acidified form of bacteriorhodopsin and its 9-cis derivative in purple membrane at low temperatures. *Photochem. Photobiol.* **33**, 559–565.

[50] Chang, C.-H., Liu, S.Y., Jonas, R., Govindjee, R. (1987). The pink membrane: the stable photoproduct of deionized purple membrane. *Biophys. J.* **52**, 617–623.

[51] Tallent, J., Song, Q.W., Li, Z., Stuart, J., Birge, R.R. (1996). Effective photochromic nonlinearity of dried blue-membrane bacteriorhodopsin films. *Opt. Lett.* **21**, 1339–1341.

[52] Tallent, J.R., Stuart, J.A., Song, Q.W., Schmidt, E.J., Martin, C.H., Birge, R.R. (1998). Photochemistry in dried polymer films incorporating the deionized blue membrane form of bacteriorhodopsin. *Biophys. J.* **75**, 1619–1634.

[53] Cladera, J., Galisteo, M.L., Duñach, M., Mateo, P.L., Padrós, E. (1988). Thermal denaturation of deionized and native purple membranes. *Biochim. Biophys. Acta* **943**, 148–156.

[54] Kresheck, G.C., Lin, C.T., Williamson, L.N., Mason, W.R., Jang, D.-J., El-Sayed, M.A. (1990). The thermal stability of native, delipidated, deionized and regenerated bacteriorhodopsin. *J. Photochem. Photobiol., B* **7**, 289–302.

[55] Mogi, T., Stern, L.J., Marti, T., Chao, B.H., Khorana, H.G. (1988). Aspartic acid substitutions affect proton translocation by bacteriorhodopsin. *Proc. Natl. Acad. Sci. USA* **85**, 4148–4152.

[56] Millerd, J.E., Rohrbacher, A., Brock, N.J., Chau, C.-K., Smith, P., Needleman, R. (1999). Improved sensitivity in blue-membrane bacteriorhodopsin films. *Opt. Lett.* **24**, 1355–1357.

[57] Turner, G.J., Miercke, L.J.W., Thorgeirsson, T.E., Kliger, D.S., Betlach, M.C., Stroud, R.M. (1993). Bacteriorhodopsin D85N: three spectroscopic species in equilibrium. *Biochemistry* **32**, 1332–1337.

[58] Tittor, J., Schweiger, U., Oesterhelt, D., Bamberg, E. (1994). Inversion of proton translocation in bacteriorhodopsin mutants D85N, D85T, and D85,96N. *Biophys. J.* **67**, 1682–1690.

[59] Liu, S.Y., Ebrey, T.G. (1987). The quantum efficiency for the interphotoconversion of the blue and pink forms of purple membrane. *Photochem. Photobiol.* **46**, 263–267.

[60] Ohtani, H., Kobayashi, T., Iwai, J., Ikegami, A. (1986). Picosecond and nanosecond spectroscopies of the photochemical cycles of acidified bacteriorhodopsin. *Biochemistry* **25**, 3356–3363.

[61] Fischer, U.C., Towner, P., Oesterheldt, D. (1981). Light induced isomerization, at acidic pH, initiates hydrolysis of bacteriorhodopsin to bacterio-opsin and 9-cis-retinal. *Photochem. Photobiol.* **33**, 529–537.

[62] Downie, J.D., Timuçin, D.A., Smithey, D.T., Crew, M. (1998). Long holographic lifetimes in bacteriorhodopsin films. *Opt. Lett.* **23**, 730–732.

[63] Bunkin, F.V., Vsevolodov, N.N., Druzhko, A.B., Mitsner, B.I., Prokhorov, A.M., Savranskii, V.V., Tkachenko, N.W., Shevchenko, T.B. (1981). Diffraction efficiency of bacteriorhodopsin and its analogs. *Sov. Tech. Phys. Lett.* **7**, 630–631.

[64] Bazhenov, V.Y., Soskin, M.S., Taranenko, V.B. (1987). Holographic recording by continuous illumination in a suspension of purple membranes of halobacteria. *Sov. Tech. Phys. Lett.* **13**, 382–384.

[65] Birge, R.R. (1990). Photophysics and molecular electronic applications of the rhodopsins. *Annu. Rev. Phys. Chem.* **41**, 683–733.

[66] Thoma, R., Hampp, N., Bräuchle, C., Oesterhelt, D. (1991). Bacteriorhodopsin films as spatial light modulators for nonlinear optical filtering. *Opt. Lett.* **16**, 651–653.

[67] Renner, T. , Hampp, N. (1992). Bacteriorhodopsin-films for dynamic time average interferometry. *Opt. Commun.* **96**, 142–149.

[68] Loudon, R. (1973). *The quantum theory of light*. Oxford, England: Clarendon.

[69] Kogelnik, H. (1969). Coupled wave theory for thick hologram gratings. *Bell Syst. Tech. J.* **48**, 2909–2947.

[70] Birge, R.R., Parsons, B., Song, Q.W., Tallent, J.R. (1997) Protein-based three-dimensional memories and associative processors. In: Ratner, M.A., Jortner, J. (Eds.) *Molecular Electronics*, Blackwell Science Ltd.: Oxford, England. pp. 439–471.

[71] Wise, K.J., Gillespie, N.B., Stuart, J.A., Krebs, M.P., Birge, R.R. (2002). Optimization of bacteriorhodopsin for bioelectronic devices. *Trends Biotechnol.* **20**, 387–394.

[72] Hillebrecht, J.R., Koscielecki, J.F., Wise, K.J., Marcy, D.L., Tetley, W., Rangarajan, R., Sullivan, J., Brideau, M., Krebs, M.P., Stuart, J.A., Birge, R.R. (2005). Optimization of Protein-Based Volumetric Optical Memories and Associative Processors by Using Directed Evolution. *NanoBiotechnology* **1**, 141–152.

[73] Hillebrecht, J.R., Wise, K.J., Birge, R.R. (2004). Directed evolution of bacteriorhodopsin for device applications. *Methods Enzymol.* **388**, 333–347.

[74] Dalby, P.A. (2003). Optimising enzyme function by directed evolution. *Curr. Opin. Struct. Biol.* **13**, 500–505.

[75] Gershenson, A., Arnold, F.H. (2000). Enzyme stabilization by directed evolution. *Genet. Eng.* **22**, 55–76.

[76] Chartrain, M., Salmon, P.M., Robinson, D.K., Buckland, B.C. (2000). Metabolic engineering and directed evolution for the production of pharmaceuticals. *Curr. Opin. Biotechnol.* **11**, 209–214.

[77] Arnold, F.H. (1998). Design by directed evolution. *Acc. Chem. Res.* **31**, 125–131.

[78] Arnold, F. , Moore, J.C. (1997). Optimizing industrial enzymes by directed evolution. *Adv. Biochem. Eng.* **58**, 1–14.